Preparation of Low Grain Boundary Perovskite Crystals with Excellent Performance: The Inhibition of Ammonium Iodide

Feng Gao,* Ke Liu, Ruzhou Cheng, Xi Zhou, Xiaoting Deng, Shaofeng Yin, and Shu Jiang
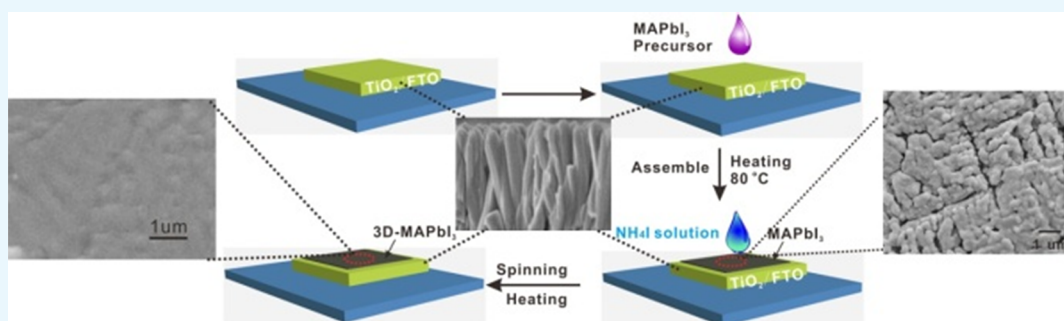
Read Online

ACCESS | Metrics & More | Article Recommendations | SI Supporting Information

ABSTRACT: For the study, we prepared a low grain boundary three-dimensional $CH_3NH_3PbI_3$ crystal (3D-MAPbI$_3$) on TiO$_2$ nanoarrays by inhibition of ammonium iodide and discussed the formation mechanism of the crystal. Based on the 3D-MAPbI$_3$ crystal, solar cells showed modified performance with a power conversion efficiency (PCE) of up to 19.3%, which increases by 36.8% in contrast to the counterparts. We studied the internal photocurrent conversion process. The highest external quantum efficiency is up to 92%, and the electron injection efficiency is remarkably facilitated where the injection time decreases by 37.8% compared to the control group. In addition, based on 3D-MAPbI$_3$, solar cells showed excellent air stability, which possesses 78.3% of the initial PCE, even though they were exposed to air for 30 days. Our results demonstrate a promising approach for the fabrication of perovskite solar cells with high efficiency and stability.

1. INTRODUCTION

Organic−inorganic hybrid perovskites have been considered as potential materials in various fields due to their special chemical structures and distinctive properties.[1−5] Since the first methylammonium lead halide perovskite ($CH_3NH_3PbX_3$, X = Br or I) in an electrolyte-based dye-sensitized solar cell was reported, scientists have researched the perovskite-based photovoltaic devices widely. Up to now, based on perovskite materials, solar cells have achieved outstanding improvements with a power conversion efficiency (PCE) reaching 25.6%.[1,6−20] The increasing device PCE heralds a new rapid development era of solar cells.

One of the main issues that hinder the development of perovskite solar cells is poor stability.[21−25] To overcome the difficulty, numerous efforts were devoted to improve the interface of the device, including developing various new electron transport materials (ETMs),[26−30] hole transport materials (HTMs),[31−35] and prepared all-inorganic solar cells.[20,36] Scientists expect using various carrier materials to improve the performance and even the stability. However, very few of the reported materials have been able to achieve gratifying stability. In fact, the general engineering of the interface facilitates the charging transfer behavior by providing effective charging transport channels.[18,28,37−40] The trans-

porting process of the carrier, especially the transporting speed (injection rate) between the donor and the receiver, has not been greatly improved.

In addition, obtained by the one-step method, perovskite crystals usually have many morphologic defects because of the heterogeneous growth during the evaporation of the solvents. For perovskite, during the complete transformation from precursor materials to crystals, the morphology of the film presents a large number of pinhole defects, which is harmful to the performance of the device. To overcome the obstacle, a great variety of traditional technologies were attempted preliminarily, such as the roll-to-roll method, doctor-blading process, spray coating, inkjet printing, slot-die printing, and so on.[41−46] However, the perovskite materials obtained by these methods are either too expensive or poor on the performance, which makes it difficult to popularize in reality.

In addition, there are many defects in perovskite crystals synthesized by chemical methods. These defects are harmful to the inner carrier transport of the device. Therefore, as for perovskite, to reduce or repair the defects in the crystal effectively has become one of the key challenges. In previous reports, synthesized by the gas phase method, perovskite can reduce the crystal defects[47−49] effectively. However, there are no suitable gas phase methods to synthesize low-defect perovskite crystals except for the traditional chemical vapor deposition (CVD) method, which is reported to be the main one,[13,47] but this kind of method has many disadvantages, such as high energy consumption, high price, and inability to be applied or promoted.[50] In view of this, scientists gradually developed and utilized different gas phase methods, such as the spray deposition method,[51,52] gas post-treatment,[53] gas-assisted crystallization,[54] and so on. However, the obvious disadvantage of these methods is the simple use of methyl ammonia gas for repair. It has not been well studied on controlling the process of growth to improve the morphology and structure of crystals.

Hereinafter, we reported a three-dimensional (3D) perovskite crystal on TiO$_2$ nanoarrays (TiO$_2$-NAs) with low grain boundaries by introducing ammonium iodide into the film. We also studied the formation process and defect repair mechanism of the crystal. Consequently, we reported 3D-MAPbI$_3$-based solar cells with improved performance and air stability. We also discussed the reasons for the improvement on the performance of the device. Notably, the electron transport layer is the TiO$_2$ array rather than mesoporous TiO$_2$. The main reasons for choosing the TiO$_2$ nanoarray as the ETM are as follows: (i) TiO$_2$ nanoarrays have good single-crystal properties and one-dimensional phase extractions, which can provide more contact sites and effective charging transport channels for fast electron transports due to the high uniform structures;[27] (ii) there are almost no deep insights into the healing process upon the perovskite/two-dimensional nanoarray interface; (iii) the mesoporous TiO$_2$ (m-TiO$_2$) film is normally used for the ETM in perovskite solar cells to increase the contact area,[55] but the crystallinity and the surface area of such TiO$_2$ thin films are not satisfactory.[15] Additionally, by using the simple spin-coating methods, perovskite crystals formed on mesoporous TiO$_2$ films obtain two-dimensional (2D) flat films, which reduce the contact interface between perovskite and TiO$_2$ films as well.

2. EXPERIMENTAL SECTION

2.1. Materials and Methods. All the materials were bought from commercial sources for use. We recorded the UV−vis measurements to test the absorption properties of the samples (Agilent Cary 300) and X-ray diffraction to test the crystal of the samples (D/MAX 2500, Cu Kα radiation, λ = 1.5405 Å). We characterized the morphology by transmission electron microscopy (TEM) measurements (Tecnai G2 F20 S-TWIN transmission electron microscope) and scanning electron microscopy (SEM) measurements (JEOL S-4800 field-emission scanning electron microscope). Time-resolved photoluminescence measurements were performed on a fluorescence spectrometer (FLS980, excitation source: 560 nm). The obtained decay curves were fitted with exponential functions ($\chi^2 = 0.9−1.1$).

2.2. Preparation of TiO$_2$ Nanoarrays. We prepared the TiO$_2$ nanoarrays by using hydrothermal methods.[27] Typically, we added 50 mL of 37% HCl and 50 mL of distilled water into a 250 mL flask with stirring for 15 min to form homogeneous

solutions. Then, we transferred the solutions into an FTO-embedded Teflon-lined hydrothermal reaction vessel. Afterward, we added 1 mL of isopropyl titanate into the vessel and sonicated the mixture for 5 min. Finally, we heated the vessel at 180 °C for 90 min to obtain the TiO$_2$ nanoarrays. For comparison, we prepared m-TiO$_2$ by referring to a previous report.[56]

2.3. Preparation of MAPbI$_3$ Precursor Solution. We synthesized CH$_3$NH$_3$I by the one-step method in the literature.[57] Methylamine (24 mL, 33% in absolute ethanol) was reacted with hydroiodic acid (10 mL, 57% in water) under a nitrogen atmosphere in 100 mL of ethanol for 2 h. After the evaporation of the mixture, a white-colored powder was formed to obtain the CH$_3$NH$_3$I crystal. We prepared the MAPbI$_3$ precursor solution by blending 0.463 g of PbI$_2$ and 0.447 g of CH$_3$NH$_3$I (mole ratio 1:3) in 3 mL of DMF solution.

2.4. Fabrication and Characterization of the Device. First, we added 0.1 mL of MAPbI$_3$ precursor solution onto the TiO$_2$-NAs/FTO thin film and directly annealed at 80 °C for 30 min under an air atmosphere to assemble the MAPbI$_3$ crystal. Then, we spin-coated 50 μL of NH$_4$I in ethanol (0.1 M) onto the films and heated at 60 °C for 12 h to form a uniform film (the synthesis process is displayed in Figure 1).
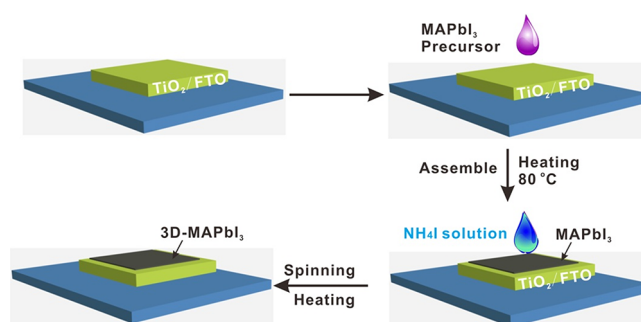

Figure 1. Synthesis process of the 3D-MAPbI$_3$ crystal.

After that, we spin-coated a chlorobenzene solution containing 68 mM Spiro-MeOTAD, 55 mM *tert*-butylpyridine, and 9 mM lithium bis(trifluoromethylsyfonyl)imide salt on the active layer at a rate of 2000 rpm for 40 s. Finally, we deposited 200 nm Au onto the Spiro-MeOTAD surface (a device area of 0.12 cm^2). We measured the current−voltage (J−V) characteristics of the devices on a solar simulator under a simulated AM1.5G spectrum at 100 mW cm^{-2} (Newport Oriel Sol 2A) and the external quantum efficiency (EQE) of the devices to test the inner photocurrent (QTest Station 500 USA).

3. RESULTS AND DISCUSSION

Figure 2a shows the top-view SEM image of the untreated MAPbI$_3$ crystal on TiO$_2$-NAs. MAPbI$_3$ is rough with lots of holes, and the crystal structure is loose. However, after 3 h of treatment with NH$_4$I, the perovskite crystals began to aggregate and grow into large films (Figure 2b). When the treatment continued for 24 h, the perovskite crystal was restored to a more complete dense layer (Figure 2c). This indicates that NH$_4$I possesses the ability to repair the crystal into a block film. Figure 2d shows the cross-sectional image of NH$_4$I-treated perovskite on TiO$_2$-NAs. Obviously, the TiO$_2$ nanoarray has fully penetrated the perovskite crystals and the thickness of the compact perovskite on TiO$_2$-NAs is calculated
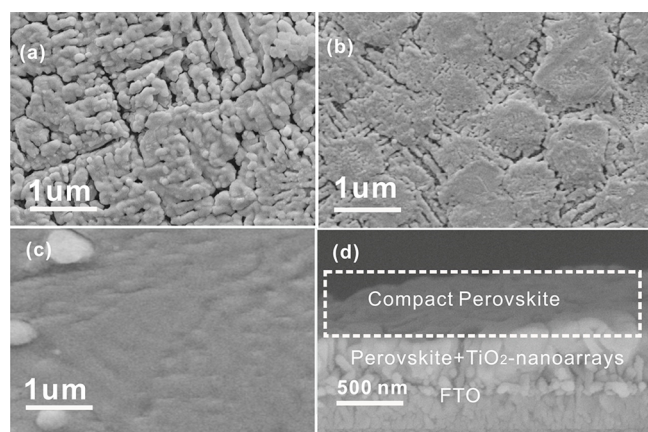
Figure 2. (a) Top-view SEM image of MAPbI$_3$ on TiO$_2$-NA films without ammonium iodide; (b) MAPbI$_3$ on TiO$_2$-NA films treated with NH$_4$I for 3 h; (c) MAPbI$_3$ on TiO$_2$-NA films treated with NH$_4$I for 24 h; (d) cross-sectional SEM images of MAPbI$_3$ films on TiO$_2$-NAs after NH$_4$I treatment for 24 h.

to be about 500−600 nm. Thus, the crystal forms a dense, smooth, and uniform three-dimensional structure. However, the MAPbI$_3$ crystal on TiO$_2$-NAs without NH$_4$I treatment (Figure S1) is rather rough with lots of grain boundaries and not completely filled in TiO$_2$-NAs. Notably, although grain boundaries are still observed on the surface of 3D-MAPbI$_3$ crystals, the number has been greatly reduced.

Figure 3a and Figure 3b show the SEM and TEM images of the as-synthesized TiO$_2$ nanoarrays, respectively. The average diameter of the nanorods is estimated to be 50−80 nm, and the length is about 500 nm. Figure 3c shows the corresponding high-resolution TEM (HRTEM) of the TiO$_2$ nanoarrays. The interspace (0.335 nm) of the crystal is the reflection of the rutile TiO$_2$ (101) plane.[27] We recorded the structures by XRD patterns (Figure 3d). TiO$_2$-NAs/FTO showed three peaks at 26.3, 35.8, and 37.7°, which agrees well with rutile TiO$_2$.[58] For the CH$_3$NH$_3$PbI$_3$ crystals, there are three new peaks that appeared at 14.2, 28.5, and 31.8° in both of the 3D-MAPbI$_3$ films before and after the NH$_4$I treatment, which can be

attributed to the (110), (220), and (310) planes, respectively.[59] It is worth noticing that all the peak intensities in the 3D-MAPbI$_3$ films after the NH$_4$I treatment are extremely enhanced. This means that the crystallized process that occurred in the healing process is better. The XRD peak at 52° in all films can be attributed to the subtraction of FTO. We tested the absorption spectra to distinguish the absorption features of MAPbI$_3$ films. As shown in Figure 3e, the 3D-MAPbI$_3$ crystal showed broad absorption bands at regions from 300 to 800 nm, which is in good agreement with the previous work.[60] Compared to the untreated films, the absorption intensities of 3D-MAPbI$_3$ crystals after the NH$_4$I treatment are significantly increased, indicating that a further assembly process occurs during the NH$_4$I treatment process. The formation of compact bulk crystals of perovskite should be responsible for the high absorption effects.

Based on the above results, we proposed the healing mechanism. Actually, the repairing process of the crystal is the reversible absorption/release of the MA gas.[47] Therefore, in an effective healing process, we should take two aspects into consideration: (i) the transformation of the rough film (Figure 2a) into a smooth one (Figure 2c) through self-leveling; (ii) the slow release of MA to produce a highly uniform and compact film. The whole process involves an intermediate state (HPbI$_3$) that is unstable to release a small amount of HI molecules.[49] The relative equations are as follows

$$\text{MAPbI}_3 \rightleftharpoons \text{MA} + \text{HPbI}_3 \tag{1}$$

$$\text{HPbI}_3 \rightleftharpoons \text{HI} + \text{PbI}_2 \tag{2}$$

$$\text{MA} + \text{HI} + \text{PbI}_2 \overrightarrow{} \text{MAPbI}_3 \tag{3}$$

Therefore, if we control the slow formation of intermediate products (HPbI$_3$), then the whole chemical kinetic process will be effectively controlled. According to this, we added ammonium iodide to films to destroy the dynamic equilibrium process, as shown in formula 2. The main reason for choosing ammonium iodide is that it is unstable and easy to decompose into HI and ammonia gas under heating conditions. Because of the release of HI from NH$_4$I, the equilibrium process of the chemical reaction in formula 2 moves toward the direction of
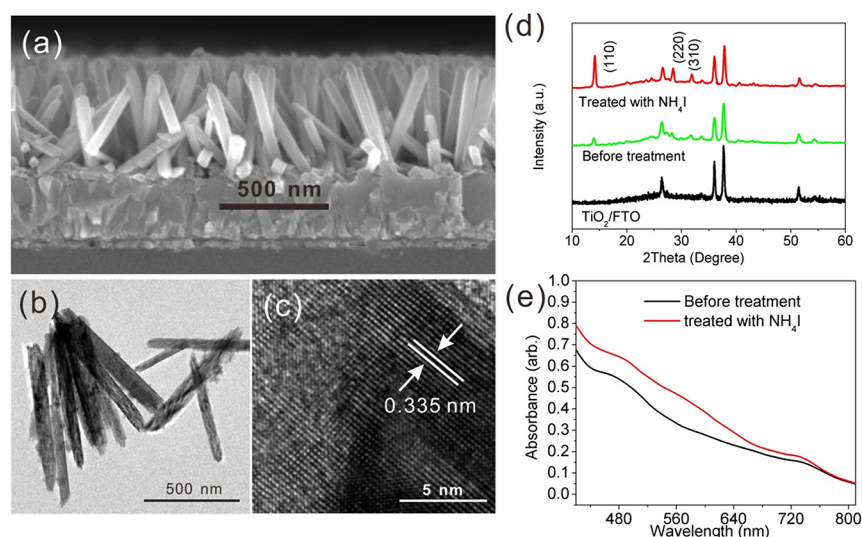

Figure 3. (a) Cross-sectional SEM, (b) TEM, and (c) HRTEM images of TiO$_2$ nanoarrays; (d) XRD patterns of MAPbI$_3$ on TiO$_2$ nanoarrays and (e) absorption spectra of MAPbI$_3$ thin films on glasses.
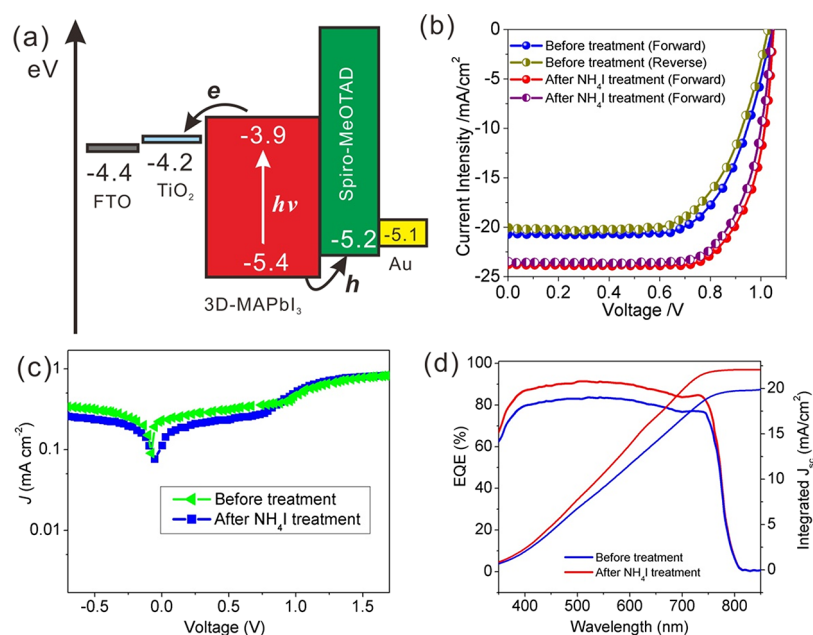
Figure 4. (a) Energy-level diagram of the solar cells based on 3D-MAPbI$_3$; (b) J–V curves and (c) dark J–V curves of the devices; (d) corresponding EQE and calculated J_{sc} of the solar cells.

reactants. This inhibited the decomposition of intermediate products and slowed down the release rate of methylamine to a certain extent. With the slow decomposition and recrystallization of perovskite molecules, new smooth, homogeneous, and large-scale perovskite films are gradually formed. The whole phase transition process can be reflected by SEM from Figure 2a−c.

It is believed that the loose structure of MAPbI$_3$ before the treatment provides an effective channel for the HI gas to enter the array, which makes the perovskite phase transitions among the titanium dioxide arrays proceed smoothly. Thus, the pore fillings of the MAPbI$_3$ molecules in TiO$_2$ nanoarrays are improved effectively. This effect can be easily observed by the cross-sectional SEM images (Figure 2d).

We fabricated the solar cells based on 3D-MAPbI$_3$. The energy-level diagrams of the solar cells are displayed in Figure 4a. All the energy levels of the materials refer to our previous work.[27] In Figure 4b, we measured the J–V curves of the champion solar cells scanned in forward and reverse directions. The 3D-MAPbI$_3$ device after the NH$_4$I treatment shows less hysteresis than the untreated device. Theoretically, in the perovskite solar cells, accumulations of chargings or ions and transferring imbalances of chargings at the interface between perovskite/ETM should be responsible for the hysteresis. Based on MAPbI$_3$ before NH$_4$I treatment, solar cells achieved performance of an open-circuit voltage (V_{oc}) of 1.04 V, a short-circuit current (J_{sc}) of 20.7 mA cm^{-2}, a fill factor (FF) of 0.65, and a PCE of 14.1%. Compared to that, based on 3D-MAPbI$_3$ after the NH$_4$I treatment, the performance of the device showed significant improvement where the V_{oc}, J_{sc}, FF, and PCE are measured to be 1.04 V, 23.8 mA cm^{-2}, 0.78, and 19.3%, respectively. The PCE increased by nearly 36.8%. In addition, the J_{sc} and FF (Table S1) based on 3D-MAPbI$_3$ are remarkably improved, indicating that 3D-MAPbI$_3$ is the photovoltaic material that has more potential. It should be noted that the V_{oc} in both of the devices is the same, suggesting that the V_{oc} is mainly dominated by the energy levels between MAPbI$_3$ and TiO$_2$ nanoarrays. To confirm the performance of

the device, we recorded 30 devices, and the average statistics are displayed in Table 1 (Figures S3 and S4). The statistical data demonstrates that the average performance has been improved for NH$_4$I-treated 3D-MAPbI$_3$-based devices.

Table 1. Average Performances of 30 Devices Based on MAPbI$_3$ Crystals

devices	V_{oc} (V)	J_{sc} (mA cm^{-2})	FF	PCE (%)
before treatment	1.04 ± 0.1	19.6 ± 2.0	0.63 ± 0.3	12.8 ± 2.1
after NH$_4$I treatment	1.04 ± 0.1	22.5 ± 1.8	0.76 ± 0.3	18.8 ± 2.0

To better understand the transfer and recombination kinetics of the charging, we studied the dark J–V data (Figure 4c), in which the curves are in good accordance with the Shockley diode equation

$$J = J_0 \left(\exp\left(\frac{qV}{nkT} \right) - 1 \right) \tag{4}$$

where n is the ideality factor, k is the Boltzmann constant, J_0 is the reverse saturation current density, and T is the temperature in Kelvin. Compared with the device before the NH$_4$I treatment, solar cells treated with NH$_4$I showed lower J_0 values and inflection points, suggesting a charging contact, which is more effective, for which the lower charging recombination and leakage at the interface between 3D-MAPbI$_3$ and TiO$_2$-NAs should be responsible.[61]

Considering the enhancement in J_{sc}, we recorded the external quantum efficiency (EQE) spectra of the solar cells (Figure 4d) to further investigate the inner photocurrent conversion efficiency. Both of the two MAPbI$_3$-based devices showed a broad band in the whole region from 400 to 800 nm. Based on MAPbI$_3$, the highest EQE before treatment is 84%, while the EQE increases dramatically for the devices based on 3D-MAPbI$_3$ after the NH$_4$I treatment. The highest EQE
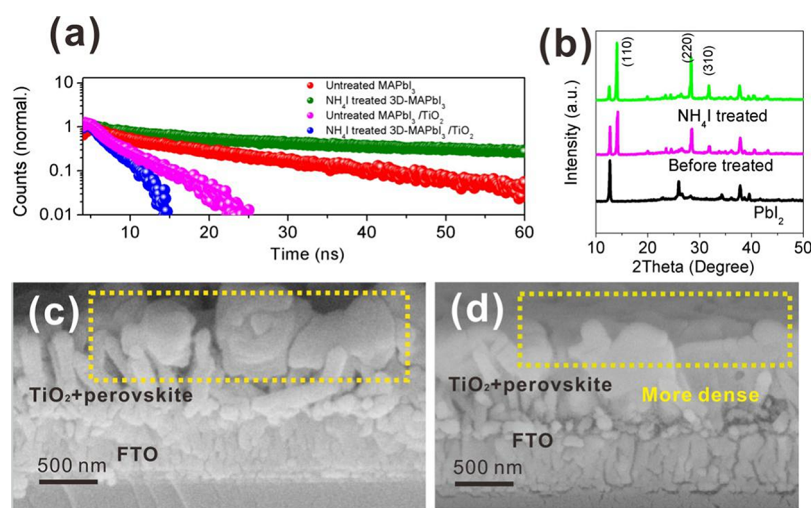
Figure 5. (a) Time-resolved photoluminescence measurements of the thin films; (b) XRD patterns of $MAPbI_3/TiO_2$ thin films under an air atmosphere for 30 days; (c, d) SEM images of the thin films before and after the NH_4I treatment under an air atmosphere for 30 days.

reaches 92%, indicating the improvement of J_{sc}. The integrated J_{sc} values from the EQE-based devices for $MAPbI_3$ before and after the NH_4I treatment are calculated to be 19.9 and 23.1 mA cm^2, respectively, which are quite consistent with the $J-V$ curves.

The resistance (R_s) of the device mainly reflects the FF. Generally speaking, a lower R_s indicates a higher FF. To conform the J_{sc} as well as the FF, we got deep investigations in the resistance of the series by the typical equation (eq 1),[62] where I_L and I_0 represent the photocurrent ($n = 1$) and dark saturation current (reverse polarization), respectively. q, T, K, and V are the values of the charging, absolute temperature, Boltzmann constant, and bias potential, respectively.

$$I = I_L - I_0 \exp\left(\frac{q(V + IR_s)}{nkT}\right) \tag{5}$$

Based on $MAPbI_3$ before and after NH_4I treatment, the R_s values of the devices are calculated to be 9.55 and 4.6 $\Omega\ cm^2$. The change in R_s is likely to be related to the structure of the perovskite. In heterostructure solar cells, the grain boundaries have strong influences on performance parameters, and R_s increases with increasing numbers of grain boundaries. The 3D-$MAPbI_3$ solar cells are ascribed to the low R_s, probably as a result of there being fewer grain boundaries.[1]

To study the characteristics of the charging transport, we recorded the time-resolved photoluminescence spectra (Figure 5a). For the pure $MAPbI_3$ thin films before and after the NH_4I treatment, we measured the lifetimes to be 14.2 and 18.1 ns, respectively. The longer lifetime in 3D-$MAPbI_3$ thin films after the NH_4I treatment suggests a longer survival time of the exciton. In addition, we calculated the charging transfer time (τ_{CT}) by a typical formula (formula 1) $\tau_{film} = 1/\tau_{MAPbI3} + 1/\tau_{CT}$,[63] where the τ_{film} and τ_{MAPbI3} are the decay lifetimes of $MAPbI_3$ on TiO_2 nanoarrays and pure $MAPbI_3$ films, respectively. The τ_{CT} for $MAPbI_3$ on TiO_2 nanoarrays before the treatment is estimated to be 15.0 ns, while the 3D-$MAPbI_3$ crystal after the NH_4I treatment shows a short lifetime of 9.5 ns (Table 2), which indicates that the electron injection between 3D-$MAPbI_3$ and the layer of TiO_2 nanoarrays is significantly facilitated, and the injection time is improved by 37.8%.

Table 2. Photoluminescence Lifetimes Measured for Pure $MAPbI_3$ Thin Films and 3D-$MAPbI_3$ Thin Films on TiO_2 Nanoarrays (τ_{film}) and the Estimated Transfer Time of the Charging Carrier (τ_{CT})

thin films on glass/FTO	τ_{film} (ns)	τ_{CT} (ns)
$MAPbI_3$ (before NH_4I treatment)	14.2	
$MAPbI_3$ (before NH_4I treatment)/TiO_2	7.3	15.0
3D-$MAPbI_3$ (after NH_4I treatment)	18.1	
3D-$MAPbI_3$ (after NH_4I treatment)/TiO_2	6.2	9.4

We further investigated the stability of the thin films. We recorded the XRD patterns of the crystal under an air atmosphere for 30 days (Figure 5b). For both of the $MAPbI_3$ crystals before and after the NH_4I treatment, a new XRD diffraction peak at 12.6° (PbI_2) has appeared, suggesting the decomposition of crystals. Although they are exposed to air for 30 days, the diffraction peak intensity of PbI_2 in 3D-$MAPbI_3$ crystals after the NH_4I treatment is much lower than that of $MAPbI_3$ crystals before the NH_4I treatment, indicating that the 3D-$MAPbI_3$ crystal after the NH_4I treatment possesses better air stability. To confirm that, we tested the SEM images of the $MAPbI_3$ crystal after 30 days to observe the morphology (Figure 5c,d). Obviously, crystal exposure to air for 30 days before the treatment (Figure 5c) showed a higher degree of decomposition due to a large number of grain boundaries because the crystal decomposition usually occurs at the grain boundaries. On the contrary, the NH_4I-treated crystals have better morphology stability. This observation is quite consistent with the previous discussion.

Considering the advanced stability property of the 3D-$MAPbI_3$ crystals, we remeasured the $J-V$ curves of the devices exposed to air for 30 days (Figure 6a). The device based on 3D-$MAPbI_3$ before the NH_4I treatment showed a V_{oc} of 0.99 V, a J_{sc} of 14.6 mA cm^{-2}, a FF of 0.63, and a PCE of 9.3% after exposure to air for 30 days. The PCE is 66% of the original efficiency. By contrast, the devices based on 3D-$MAPbI_3$ after the NH_4I treatment showed an enhanced performance with a V_{oc} of 1.01 V, a J_{sc} of 20.1 mA cm^{-2}, a FF of 0.74, and a PCE of 15.1%, which possesses 78.3% of the original efficiency, even though they are exposed to air for 30 days, which is much
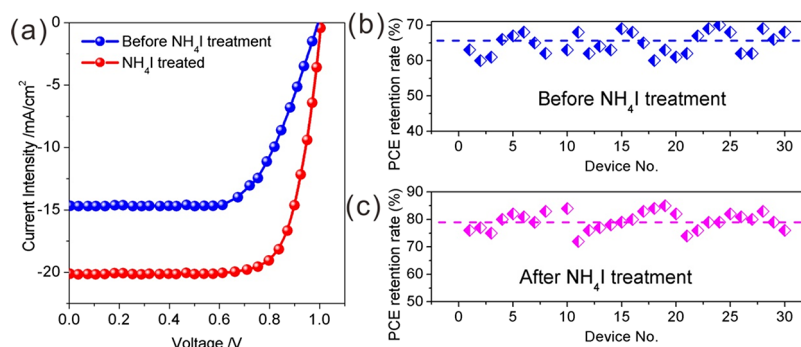
Figure 6. (a) $J-V$ curves of the devices after exposure to air for 30 days; the PCE retention rate of the devices before and after the NH$_4$I treatment (b, c) after exposure to air for 30 days.

higher than that of the device based on 3D-MAPbI$_3$ after NH$_4$I treatment.

To further investigate the PCE retention rate of the solar cells after exposure to air for 30 days, we counted 30 devices and obtained the statistics of the PCE retention rate for 3D-MAPbI$_3$ before and after the NH$_4$ treatment. For the devices based on MAPbI$_3$ before the NH$_4$ treatment, the average PCE retention rate is calculated to be 65.6%, and the highest PCE retention rate is 69%, while the average PCE retention rate for the 3D-MAPbI$_3$ devices after the NH$_4$ treatment is estimated to be 78.1%, and the highest PCE retention is measured to be 85%. The advanced air stability of the NH$_4$I-treated solar cells suggests the potential application of 3D-MAPbI$_3$ in photovoltaic devices.

4. CONCLUSIONS

In summary, we prepared the 3D-MAPbI$_3$ crystal with low grain boundaries on TiO$_2$ nanoarrays as well as proposed and discussed the formation mechanism. The inhibition of ammonium iodide came up for the first time. Solar cells based on 3D-MAPbI$_3$ after the NH$_4$I treatment showed a modified performance as high as 17.6%, which increased by 36.8% in contrast to the counterpart. Facts proved that, for the device, based on NH$_4$I-treated 3D-MAPbI$_3$ films, the EQE (92%) is significantly improved. Moreover, the electron injection between the 3D-MAPbI$_3$ layers after the NH$_4$I treatment and TiO$_2$ nanoarrays is remarkably facilitated. The total time of the electron injection decreased by 37.8% compared to the control group. In addition, based on 3D-MAPbI, solar cells showed excellent air stability, and the device possesses 78.3% of the initial PCE, even though it is exposed to air for 30 days. The devices based on NH$_4$I-treated 3D-MAPbI$_3$ showed an average PCE retention rate of 78.1%, much higher than the counterpart. In view of the above results, it is believed that the inhibition of ammonium iodide has positive effects on the phase transformation and film formation for perovskite crystals, which is adopted to produce advanced materials for fabrication of perovskite photovoltaic devices with high efficiency and stability.

ASSOCIATED CONTENT

⑤ Supporting Information

The Supporting Information is available free of charge at https://pubs.acs.org/doi/10.1021/acsomega.1c01260.

The SEM images of TiO$_2$ nanoarrays and m-TiO$_2$-based perovskite, statistic distribution of photovoltaic metrics, and table containing device performance (PDF)

AUTHOR INFORMATION

Corresponding Author

Feng Gao − *College of Food and Chemical Engineering, Shaoyang University, Shaoyang 422000, People's Republic of China;* ⓘ orcid.org/0000-0001-5273-7627; Email: gaofeng137@tju.edu.cn

Authors

Ke Liu − *College of Food and Chemical Engineering, Shaoyang University, Shaoyang 422000, People's Republic of China*

Ruzhou Cheng − *College of Food and Chemical Engineering, Shaoyang University, Shaoyang 422000, People's Republic of China*

Xi Zhou − *College of Food and Chemical Engineering, Shaoyang University, Shaoyang 422000, People's Republic of China;* ⓘ orcid.org/0000-0002-6736-7160

Xiaoting Deng − *College of Food and Chemical Engineering, Shaoyang University, Shaoyang 422000, People's Republic of China*

Shaofeng Yin − *College of Food and Chemical Engineering, Shaoyang University, Shaoyang 422000, People's Republic of China*

Shu Jiang − *College of Food and Chemical Engineering, Shaoyang University, Shaoyang 422000, People's Republic of China*

Complete contact information is available at:
https://pubs.acs.org/10.1021/acsomega.1c01260

Notes

The authors declare no competing financial interest.

ACKNOWLEDGMENTS

REFERENCES

(1) Im, J. H.; Jang, I. H.; Pellet, N.; Grätzel, M.; Park, N. G. Growth of CH$_3$NH$_3$PbI$_3$ cuboids with controlled size for high-efficiency perovskite solar cells. *Nat. Nanotechnol.* **2014**, *9*, 927−932.

(2) Green, M. A.; Ho-Baillie, A.; Snaith, H. J. The emergence of perovskite solar cells. *Nat. Photon.* **2014**, *8*, 506.

(3) Eperon, G. E.; Burlakov, V. M.; Docampo, P.; Goriely, A.; Snaith, H. J. Morphological Control for High Performance, Solution-Processed Planar Heterojunction Perovskite Solar Cells. *Adv. Funct. Mater.* **2014**, *24*, 151−157.

(4) Qin, P.; Paek, S.; Dar, M. I.; Pellet, N.; Ko, J.; Grätzel, M.; Nazeeruddin, M. K. Perovskite solar cells with 12.8% efficiency by using conjugated quinolizino acridine based hole transporting material. *J. Am. Chem. Soc.* **2014**, *136*, 8516−8519.

(5) Zhao, Y.; Zhu, K. Efficient planar perovskite solar cells based on 1.8 eV band gap $CH_3NH_3PbI_2Br$ nanosheets via thermal decomposition. *J. Am. Chem. Soc.* **2014**, *136*, 12241−12244.

(6) Zhang, P.; Wu, J.; Zhang, T.; Wang, Y.; Liu, D.; Chen, H.; Ji, L.; Liu, C.; Ahmad, W.; Chen, Z. D.; Li, S. Perovskite Solar Cells with ZnO Electron-Transporting Materials. *Adv. Mater.* **2018**, *30*, 1703737.

(7) Zhang, Y.; Zhou, Z.; Ji, F.; Li, Z.; Cui, G.; Gao, P.; Oveisi, E.; Nazeeruddin, M. K.; Pang, S. Trash into Treasure: delta-$FAPbI_3$ Polymorph Stabilized $MAPbI_3$ Perovskite with Power Conversion Efficiency beyond 21. *Adv. Mater.* **2018**, *30*, No. e1707143.

(8) Zhang, J.; Tong, T.; Zhang, L.; Li, X.; Zou, H.; Yu, J. Enhanced Performance of Planar Perovskite Solar Cell by Graphene Quantum Dot Modification. *ACS Sustainable Chem. Eng.* **2018**, *6*, 8631−8640.

(9) Zhu, H.-C.; Li, C.-F.; Fu, Z.-H.; Wei, S.-S.; Zhu, X.-F.; Zhang, J. Increasing the open-circuit voltage and adsorption stability of squaraine dye binding onto the TiO_2 anatase (1 0 1) surface via heterocyclic anchoring groups used for DSSC. *Appl. Surf. Sci.* **2018**, *455*, 1095−1105.

(10) Zhou, H.; Chen, Q.; Li, G.; Luo, S.; Song, T. B.; Duan, H. S.; Hong, Z.; You, J.; Liu, Y.; Yang, Y. Photovoltaics. Interface engineering of highly efficient perovskite solar cells. *Science* **2014**, *345*, 542−546.

(11) Bi, D.; Yi, C.; Luo, J.; Décoppet, J.-D.; Zhang, F.; Zakeeruddin, S. M.; Li, X.; Hagfeldt, A.; Grätzel, M. Polymer-templated nucleation and crystal growth of perovskite films for solar cells with efficiency greater than 21%. *Nat. Energy* **2016**, *1*, 16142.

(12) Jiang, Q.; Zhang, L.; Wang, H.; Yang, X.; Meng, J.; Liu, H.; Yin, Z.; Wu, J.; Zhang, X.; You, J. Enhanced electron extraction using SnO_2 for high-efficiency planar-structure HC(NH2)2PbI3-based perovskite solar cells. *Nat. Energy* **2017**, *2*, 16177.

(13) Liu, M.; Johnston, M. B.; Snaith, H. J. Efficient planar heterojunction perovskite solar cells by vapour deposition. *Nature* **2013**, *501*, 395−398.

(14) Bush, K. A.; Palmstrom, A. F.; Yu, Z. J.; Boccard, M.; Cheacharoen, R.; Mailoa, J. P.; McMeekin, D. P.; Hoye, R. L. Z.; Bailie, C. D.; Leijtens, T.; Peters, I. M.; Minichetti, M. C.; Rolston, N.; Prasanna, R.; Sofia, S.; Harwood, D.; Ma, W.; Moghadam, F.; Snaith, H. J.; Buonassisi, T.; Holman, Z. C.; Bent, S. F.; McGehee, M. D. 23.6%-efficient monolithic perovskite/silicon tandem solar cells with improved stability. *Nat. Energy* **2017**, *2*, 17009.

(15) Aeineh, N.; Castro-Méndez, A.-F.; Rodriguez-Cantó, P. J.; Abargues, R.; Hassanabadi, E.; Suarez, I.; Behjat, A.; Ortiz, P.; Martinez-Pastor, J. P.; Mora-Seró, I. Optical Optimization of the TiO_2 Mesoporous Layer in Perovskite Solar Cells by the Addition of SiO_2 Nanoparticles. *ACS Omega* **2018**, *3*, 9798−9804.

(16) Min, H.; Kim, M.; Lee, S.-U.; Kim, H.; Kim, G.; Choi, K.; Lee, J. H.; Seok, S. I. Efficient, stable solar cells by using inherent bandgap of α-phase formamidinium lead iodide. *Science* **2019**, *366*, 749−753.

(17) Wan, X.; Yu, Z.; Tian, W.; Huang, F.; Jin, S.; Yang, X.; Cheng, Y.-B.; Hagfeldt, A.; Sun, L. Efficient and stable planar all-inorganic perovskite solar cells based on high-quality CsPbBr3 films with controllable morphology. *J. Energy Chem.* **2020**, *46*, 8−15.

(18) Jeong, J.; Kim, M.; Seo, J.; Lu, H.; Ahlawat, P.; Mishra, A.; Yang, Y.; Hope, M. A.; Eickemeyer, F. T.; Kim, M.; Yoon, Y. J.; Choi, I. W.; Darwich, B. P.; Choi, S. J.; Jo, Y.; Lee, J. H.; Walker, B.; Zakeeruddin, S. M.; Emsley, L.; Rothlisberger, U.; Hagfeldt, A.; Kim, D. S.; Grätzel, M.; Kim, J. Y. Pseudo-halide anion engineering for α-FAPbI₃ perovskite solar cells. *Nature* **2021**, *592*, 381.

(19) Taylor, A. D.; Sun, Q.; Goetz, K. P.; An, Q.; Schramm, T.; Hofstetter, Y.; Litterst, M.; Paulus, F.; Vaynzof, Y. A general approach to high-efficiency perovskite solar cells by any antisolvent. *Nat. Commun.* **2021**, *12*, 1878.

(20) Cho, N.-K.; Na, H.-J.; Yoo, J.; Kim, Y. S. Long-term stability in γ-CsPbI3 perovskite via an ultraviolet-curable polymer network. *Communications Materials* **2021**, *2*, 30.

(21) Christians, J. A.; Habisreutinger, S. N.; Berry, J. J.; Luther, J. M. Stability in Perovskite Photovoltaics: A Paradigm for Newfangled Technologies. *ACS Energy Lett.* **2018**, 2136−2143.

(22) Gholipour, S.; Saliba, M. From Exceptional Properties to Stability Challenges of Perovskite Solar Cells. *Small* **2018**, *14*, 1802385.

(23) Saidaminov, M. I.; Kim, J.; Jain, A.; Quintero-Bermudez, R.; Tan, H.; Long, G.; Tan, F.; Johnston, A.; Zhao, Y.; Voznyy, O.; Sargent, E. H. Suppression of atomic vacancies via incorporation of isovalent small ions to increase the stability of halide perovskite solar cells in ambient air. *Nat. Energy* **2018**, *3*, 648−654.

(24) Yang, S.; Fu, W.; Zhang, Z.; Chen, H.; Li, C.-Z. Recent advances in perovskite solar cells: efficiency, stability and lead-free perovskite. *J. Mater. Chem. A* **2017**, *5*, 11462−11482.

(25) Wang, R.; Mujahid, M.; Duan, Y.; Wang, Z.-K.; Xue, J.; Yang, Y. A Review of Perovskites Solar Cell Stability. *Adv. Funct. Mater.* **2019**, *29*, 1808843.

(26) Yi, C.; Li, X.; Luo, J.; Zakeeruddin, S. M.; Grätzel, M. Perovskite Photovoltaics with Outstanding Performance Produced by Chemical Conversion of Bilayer Mesostructured Lead Halide/TiO_2 Films. *Adv. Mater.* **2016**, *28*, 2964−2970.

(27) Gao, F.; Dai, H.; Pan, H.; Chen, Y.; Wang, J.; Chen, Z. Performance enhancement of perovskite solar cells by employing TiO2 nanorod arrays decorated with CuInS2 quantum dots. *J. Colloid Interface Sci.* **2018**, *513*, 693−699.

(28) Wang, J. T.-W.; Ball, J. M.; Barea, E. M.; Abate, A.; Alexander-Webber, J. A.; Huang, J.; Saliba, M.; Mora-Sero, I.; Bisquert, J.; Snaith, H. J.; Nicholas, R. J. Low-temperature processed electron collection layers of graphene/TiO_2 nanocomposites in thin film perovskite solar cells. *Nano Lett.* **2014**, *14*, 724.

(29) Han, G. S.; Song, Y. H.; Jin, Y. U.; Lee, J.-W.; Park, N.-G.; Kang, B. K.; Lee, J.-K.; Cho, I. S.; Yoon, D. H.; Jung, H. S. Reduced Graphene Oxide/Mesoporous TiO2 Nanocomposite Based Perovskite Solar Cells. *ACS Appl. Mater. Interfaces* **2015**, *7*, 23521−23526.

(30) Ahmed, M. I.; Hussain, Z.; Khalid, A.; Amin, H. M. N.; Habib, A. Absorption enhancement in CH3NH3PbI3 solar cell using a TiO2/MoS2 nanocomposite electron selective contact. *Mater. Res. Express* **2016**, *3*, No. 045022.

(31) Lee, D. Y.; Na, S. I.; Kim, S. S. Graphene oxide/PEDOT:PSS composite hole transport layer for efficient and stable planar heterojunction perovskite solar cells. *Nanoscale* **2016**, *8*, 1513−1522.

(32) Lefrançois, A.; Luszczynska, B.; Pepin-Donat, B.; Lombard, C.; Bouthinon, B.; Verilhac, J.-M.; Gromova, M.; Faure-Vincent, J.; Pouget, S.; Chandezon, F.; Sadki, S.; Reiss, P. Enhanced charge separation in ternary $P_3HT/PCBM/CuInS_2$ nanocrystals hybrid solar cells. *Sci. Rep.* **2015**, *5*, 7768.

(33) Lv, W.; Zhu, J.; Huang, Y.; Li, Y.; Shao, Z.; Xu, Y.; Dai, S. Colloidal CuInS2 Quantum Dots as Inorganic Hole-Transporting Material in Perovskite Solar Cells. *ACS Appl. Mater. Interfaces* **2015**, *7*, 17482−17488.

(34) Seo, S.; Jeong, S.; Bae, C.; Park, N. G.; Shin, H. Perovskite Solar Cells with Inorganic Electron- and Hole-Transport Layers Exhibiting Long-Term (≈500 h) Stability at 85 °C under Continuous 1 Sun Illumination in Ambient Air. *Adv. Mater.* **2018**, *30*, 1801010.

(35) You, P.; Tang, G.; Cao, J.; Shen, D.; Ng, T. W.; Hawash, Z.; Wang, N.; Liu, C. K.; Lu, W.; Tai, Q.; Qi, Y.; Lee, C. S.; Yan, F. 2D materials for conducting holes from grain boundaries in perovskite solar cells. *Light Sci Appl* **2021**, *10*, 68.

(36) Yu, B.; Shi, J.; Tan, S.; Cui, Y.; Zhao, W.; Wu, H.; Luo, Y.; Li, D.; Meng, Q. Efficient (>20%) and Stable All-inorganic Cesium Lead Triiodide Solar Cell Enabled by Thiocyanate Molten Salts. *Angew Chem Int Ed Engl* **2021**, DOI: 10.1002/anie.202102466.

(37) Dong, Q.; Wang, M.; Zhang, Q.; Chen, F.; Zhang, S.; Bian, J.; Ma, T.; Wang, L.; Shi, Y. Discontinuous SnO_2 derived blended-interfacial-layer in mesoscopic perovskite solar cells: Minimizing electron transfer resistance and improving stability. *Nano Energy* **2017**, *38*, 358−367.

(38) Song, J.; Xu, X.; Wu, J.; Lan, Z. Low-temperature solution-processing high quality Nb-doped SnO_2 nanocrystals-based electron

transport layers for efficient planar perovskite solar cells. *Funct. Mater. Lett.* **2018**, *12*, 1850091.

(39) Yang, G.; Chen, C.; Yao, F.; Chen, Z.; Zhang, Q.; Zheng, X.; Ma, J.; Lei, H.; Qin, P.; Xiong, L.; Ke, W.; Li, G.; Yan, Y.; Fang, G. Effective Carrier-Concentration Tuning of SnO_2 Quantum Dot Electron-Selective Layers for High-Performance Planar Perovskite Solar Cells. *Adv. Mater.* **2018**, *30*, e1706023.

(40) Du, J.; Feng, L.; Guo, X.; Huang, X.; Lin, Z.; Su, J.; Hu, Z.; Zhang, J.; Chang, J.; Hao, Y. Enhanced efficiency and stability of planar perovskite solar cells by introducing amino acid to SnO2/perovskite interface. *J. Power Sources* **2020**, *455*, 227974.

(41) Li, C.; Pang, S.; Xu, H.; Cui, G. Methylamine Gas Based Synthesis and Healing Process Toward Upscaling of Perovskite Solar Cells: Progress and Perspective. *Solar RRL* **2017**, *1*, 1700076.

(42) Burwig, T.; Fränzel, W.; Pistor, P. Crystal Phases and Thermal Stability of Co-evaporated $CsPbX_3$ (X = I, Br) Thin Films. *J. Phys. Chem. Lett.* **2018**, *9*, 4808−4813.

(43) Chen, J.; Xu, J.; Xiao, L.; Zhang, B.; Dai, S.; Yao, J. Mixed-Organic-Cation $(FA)_x(MA)_{1-x}PbI_3$ Planar Perovskite Solar Cells with 16.48% Efficiency via a Low-Pressure Vapor-Assisted Solution Process. *ACS Appl. Mater. Interfaces* **2017**, *9*, 2449−2458.

(44) Leyden, M. R.; Ono, L. K.; Raga, S. R.; Kato, Y.; Wang, S.; Qi, Y. High performance perovskite solar cells by hybrid chemical vapor deposition. *J. Mater. Chem. A* **2014**, *2*, 18742−18745.

(45) Han, W.; Ren, G.; Li, Z.; Dong, M.; Liu, C.; Guo, W. Improving the performance of perovskite solar cells by surface passivation. *J. Energy Chem.* **2020**, *46*, 202−207.

(46) Ma, L.; Yan, Z.; Zhou, X.; Pi, Y.; Du, Y.; Huang, J.; Wang, K.; Wu, K.; Zhuang, C.; Han, X. A polymer controlled nucleation route towards the generalized growth of organic-inorganic perovskite single crystals. *Nat. Commun.* **2021**, *12*, 2023.

(47) Shao, Z.; Wang, Z.; Li, Z.; Fan, Y.; Meng, H.; Liu, R.; Wang, Y.; Hagfeldt, A.; Cui, G.; Pang, S. A Scalable Methylamine Gas Healing Strategy for High-Efficiency Inorganic Perovskite Solar Cells. *Angew. Chem., Int. Ed. Engl.* **2019**, *58*, 5587−5591.

(48) Nawaz, A.; Wong, K. K.; Ebenhoch, C.; Zimmermann, E.; Zheng, Z.; Akram, M. N.; Kalb, J.; Wang, K.; Fakharuddin, A.; Schmidt-Mende, L. Improving pore-filling in TiO2 nanorods and nanotubes scaffolds for perovskite solar cells via methylamine gas healing. *Solar Energy* **2018**, *170*, 541−548.

(49) Liu, Z.; Qiu, L.; Juarez-Perez, E. J.; Hawash, Z.; Kim, T.; Jiang, Y.; Wu, Z.; Raga, S. R.; Ono, L. K.; Liu, S. F.; Qi, Y. Gas-solid reaction based over one-micrometer thick stable perovskite films for efficient solar cells and modules. *Nat. Commun.* **2018**, *9*, 3880.

(50) Moser, T.; Artuk, K.; Jiang, Y.; Feurer, T.; Gilshtein, E.; Tiwari, A. N.; Fu, F. Revealing the perovskite formation kinetics during chemical vapour deposition. *J. Mater. Chem. A* **2020**, *8*, 21973−21982.

(51) Bi, Z.; Liang, Z.; Xu, X.; Chai, Z.; Jin, H.; Xu, D.; Li, J.; Li, M.; Xu, G. Fast preparation of uniform large grain size perovskite thin film in air condition via spray deposition method for high efficient planar solar cells. *Sol. Energy Mater. Sol. Cells* **2017**, *162*, 13−20.

(52) Mortan, C.; Hellmann, T.; Buchhorn, M.; d'Eril Melzi, M.; Clemens, O.; Mayer, T.; Jaegermann, W. Preparation of methyl-ammonium lead iodide $(CH_3NH_3PbI_3)$ thin film perovskite solar cells by chemical vapor deposition using methylamine gas (CH_3NH_2) and hydrogen iodide gas. *ENERGY. SCI. ENG.* **2020**, *8*, 3165−3173.

(53) Zhou, W.; Zhou, P.; Lei, X.; Fang, Z.; Zhang, M.; Liu, Q.; Chen, T.; Zeng, H.; Ding, L.; Zhu, J.; Dai, S.; Yang, S. Phase Engineering of Perovskite Materials for High-Efficiency Solar Cells: Rapid Conversion of $CH_3NH_3PbI_3$ to Phase-Pure $CH_3NH_3PbCl_3$ via Hydrochloric Acid Vapor Annealing Post-Treatment. *ACS Appl. Mater. Interfaces* **2018**, *10*, 1897−1908.

(54) Han, S.; Kim, H.; Lee, S.; Kim, C. Efficient Planar-Heterojunction Perovskite Solar Cells Fabricated by High-Through-put Sheath-Gas-Assisted Electrospray. *ACS Appl. Mater. Interfaces* **2018**, *10*, 7281−7288.

(55) Zhu, Q.; Wang, Z.; Cai, X.; Wang, W.; Wu, G.; Kong, L.; Zheng, X.; Cao, Y.; Wu, Y.; Li, X.; Wu, Z.; Kang, J. Enhanced carrier separation efficiency and performance in planar-structure perovskite

solar cells through an interfacial modifying layer of ultrathin mesoporous TiO2. *J. Power Sources* **2020**, *465*, 228251.

(56) Cho, Y.; Soufiani, A. M.; Yun, J. S.; Kim, J.; Lee, D. S.; Seidel, J.; Deng, X.; Green, M. A.; Huang, S.; Ho-Baillie, A. W. Y. Mixed 3D-2D Passivation Treatment for Mixed-Cation Lead Mixed-Halide Perovskite Solar Cells for Higher Efficiency and Better Stability. *Adv. Energy Mater.* **2018**, *8*, 1703392.

(57) Lee, M. M.; Teuscher, J.; Miyasaka, T.; Murakami, T. N.; Snaith, H. J. Efficient hybrid solar cells based on meso-superstructured organometal halide perovskites. *Science* **2012**, *338*, 643−647.

(58) Zhong, D.; Cai, B.; Wang, X.; Yang, Z.; Xing, Y.; Miao, S.; Zhang, W.-H.; Li, C. Synthesis of oriented TiO2 nanocones with fast charge transfer for perovskite solar cells. *Nano Energy* **2015**, *11*, 409−418.

(59) Qingfeng, D.; Yanjun, F.; Yuchuan, S.; Padhraic, M.; Jie, Q.; Lei, C.; Jinsong, H. Solar cells. Electron-hole diffusion lengths > 175 μm in solution-grown $CH_3NH_3PbI_3$ single crystals. *Science* **2015**, *347*, 967−970.

(60) Im, J.-H.; Kim, H.-S.; Park, N.-G. Morphology-photovoltaic property correlation in perovskite solar cells: One-step versus two-step deposition of CH3NH3PbI3. *APL Mater.* **2014**, *2*, No. 081510.

(61) Li, N.; Yan, J.; Ai, Y.; Jiang, E.; Lin, L.; Shou, C.; Yan, B.; Sheng, J.; Ye, J. A low-temperature TiO2/SnO2 electron transport layer for high-performance planar perovskite solar cells. *Sci. China Mater.* **2019**, *63*, 207−215.

(62) Gao, F.; Zheng, Q.; Zhang, Y. Stability Improvement of Perovskite Solar Cells for Application of $CuInS_2$ Quantum Dot-Modified TiO_2 Nanoarrays. *ACS Omega* **2019**, *4*, 3432−3438.

(63) Stranks, S. D.; Eperon, G. E.; Grancini, G.; Menelaou, C.; Alcocer, M. J. P.; Leijtens, T.; Herz, L. M.; Petrozza, A.; Snaith, H. J. Electron-hole diffusion lengths exceeding 1 micrometer in an organometal trihalide perovskite absorber. *Science* **2013**, *342*, 341−344.